Acoustic validation of a new code using particle wake aerodynamics and geometrically-exact beam structural dynamics

F. Nitzsche
Department of Mechanical and Aerospace Engineering
Carleton University
Ottawa, Canada

D. G. Opoku
United Technologies Research Center,
East Hartford, CT
USA

ABSTRACT

This paper describes the validation of a new code for prediction both aeroacoustic and aeroelastic behaviour of hingeless rotors. The structural component is based on a non-linear beam element model considering small strains and finite rotations, which uses a mixed variational intrinsic formulation. The aerodynamic component is built on a low-order panel method incorporating a vortex particle free-wake model. The aerodynamic and structural components are combined to form a closely coupled aeroelastic code that solves in the time-domain. The loading and thickness noise terms for the aeroacoustic calculations are calculated from the aerodynamic data using a formulation based on the Ffowcs Williams-Hawkings (FW-H) equation. The code is successfully validated for acoustic signature and BVI predictions using test cases from the HELINOISE program.

NOMENCLATURE

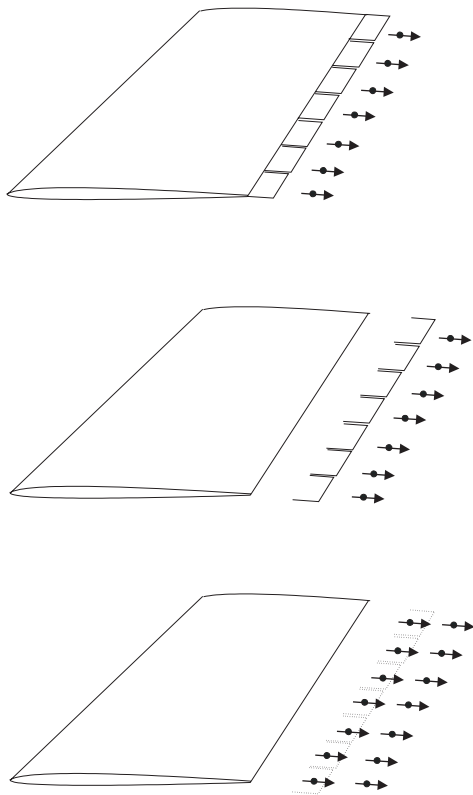|	
c	speed of sound
D	local drag
EA	blade local axial rigidity
EI_{flap}	blade local bending rigidity in the flap direction
EI_{lag}	blade local bending rigidity in the lead-lag direction
F_S, F_L	structural and load operators
GJ	blade local torsional rigidity
$H(f)$	heaviside step function
$I_{11,22,33}$	blade mass moments of inertia about the local axis per unit of length
l_i	cartesian components of the local force applied on the fluid per unit of area (i =1,2,3)
l_r	radial component of the local force applied on the fluid per unit of area
L	local lift
m	blade mass per unit of length
M	local aerodynamic pitching moment
$M_{i,r}$	Mach number (total local, radial component)
p'	total aeroacoustic perturbation pressure
p'_L	aeroacoustic perturbation pressure due to loading (dipole)
p'_T	aeroacoustic perturbation pressure due to thickness (monopole)
$\vec{r} = \vec{x} - \vec{y}$	vector defining the observer and source relative positions, respectively
$\hat{r} = \vec{r}/|\vec{r}|$	local unit vector defining the observer and source relative positions, respectively
SPL	sound pressure level, $SPL = 20\log(p'/p_{ref})$, $p_{ref} = 20\mu Pa$
t	time
T_{ij}	Lighthill stress tensor applied on the fluid elementary volume (i, j =1,2,3)
$\vec{u}$	flow velocity vector around the rotorcraft
$\vec{u}_\infty$	undisturbed flow velocity
$\vec{u}_{ext}$	imposed external flow velocity
$\vec{u}_{solid}$	flow induced velocity due to the influence of solid bodies

The development of this new code is the result of a collaboration involving the National Technical University of Athens (NTUA) in Greece, the Massachusetts Institute of Technology (MIT) in the USA, and Carleton University (Carleton) in Canada. The referred partners provided the aerodynamic, structural and acoustic components, respectively. An existing NTUA aerodynamic code – GENeral Unsteady Vortex Particle, shortly GENUVP[1], through collaboration between Carleton and NTUA, is modified in the current work to become the aerodynamic component of the new code. GENUVP has several powerful features, including the accurate modelling of wake effects, the ability to model various flight scenarios and full rotorcraft configurations. The structural component of this work is based on a slightly modified by Carleton version of a code originally developed at MIT[2], which is based on a non-linear, 'geometrically exact,' beam-element representation of the rotorblades using the mixed variational intrinsic formulation first introduced by Hodges[3]. The code aeroelastic interface to couple the aerodynamic and structural components in the time-domain was developed by Carleton and MIT. The aeroacoustic component was entirely developed at Carleton[4], based on the Ffowcs Williams-Hawkings (FW-H) equation[5]. The lifting surfaces of the blades are discretised into panel elements, each of which representing an elementary acoustic source. The total acoustic field produced by all panels is calculated based on the noise spectrum generated by replicating the aeroacoustic data retrieved after a periodic solution in the time-domain is achieved. To validate the aeroacoustic component of the new code integrated by Carleton, the HELINOISE and the NASA UH-1H experiments were used as the benchmarks. The numerical results obtained with the code, including both the aerodynamic loading and acoustic signature of the rotorblades successfully validated the new code against test cases from the HELINOISE program.

2.0 PROBLEM FORMULATION

Computational modelling of rotorcraft aeroacoustics is a unique and challenging problem. To properly model a rotorcraft, the non-linear aeroelastic interaction between several independently moving elastic bodies – the rotorblades must be captured. In addition, the influence of the rotor wake must be considered as it is of fundamental importance to predict the unsteady aerodynamic loads acting on the blades, and capture phenomena such as blade-vortex interaction (BVI) effects. These factors combined make aeroelasticity and, subsequently, aeroacoustics of rotorcraft a computationally expensive task.

2.1 Aerodynamic component

Grid-based computational fluids dynamics (CFD) codes have been used with relative success to model rotorcraft aerodynamics[6-7]. While grid-based CFD has the potential to eventually provide detailed rotorcraft aerodynamic calculations, its use is currently limited because is too computationally expensive. Due to the presence of multiple independently moving elastic bodies and a relatively large flow domain, the generation of a suitable grid for rotorcraft is laborious. In addition, grid-based CFD has the difficulty of correctly capturing essential wake effects due to numerical dissipation. An alternative approach is to use a panel method or lifting-line model, coupled with a vortex wake model for aerodynamic modelling[8-9]. Although they provide lower resolution of the flow-field than the grid-based CFD, these methods can provide an accurate prediction of the aerodynamic loading on the rotor blades in a variety of flight situations. More importantly, the prediction is obtained with computational costs that are orders of magnitude less than grid-based CFD. GENUVP is an example of such a code, based on the panel method with a vortex particle wake model for calculating the flow-field around multi-component configurations. It was first developed for wind-turbine applications[10]. The basis of

Figure 1. The formation of vortex particles from a trailing edge wake strip.

$\vec{u}_{near\text{-}wake}$	flow induced velocity due to the influence of the near-wake (attached to the aerofoil)
$\vec{u}_{far\text{-}wake}$	flow induced velocity due to the far-wake (detached from aerofoil, convected downstream)
v_i	local flow total velocity
v_n	flow normal velocity on the body surface
x	observer position vector
$\vec{x}_0$	singularity position vector
$\mathbf{X}$	state vector of structural variables: discrete measures of displacement, rotation, internal loads, moments, and selected boundary values
$\underline{X}_a$	offset between the beam reference axis and aerodynamic centre
$\underline{X}_{CG}$	offset between the beam reference axis and the centre of gravity
y	source position vector
$\delta(f)$	dirac delta function
ρ	flow density (undisturbed)
τ	'retarded' time (at which the acoustic signal was emitted)
$\vec{\omega}$	vorticity vector

1.0 INTRODUCTION

The objective of the current paper is to describe the development and initial validation of a new aeroelastic/aeroacoustic code to study noise and vibration in rotorcraft. The code interfaces separate aerodynamic and structural dynamic components. The aerodynamic component is based on a high-resolution unsteady panel method with a vortex particle model description of the free-wake. The structural component is a non-linear beam finite-element model of the rotor blades based on a mixed variational intrinsic formulation. Together, these components form a closely coupled aeroelastic code that is solved in the time domain. Data from the aerodynamic component is used to obtain acoustic results.

GENUVP is the Helmholtz decomposition principle. Using Helmholtz Principle, the flow-field around a rotorcraft can be decomposed into an irrotational part due to the presence of multiple bodies, and a rotational part due to the wakes emitted by lifting bodies. If $\vec{u}(\vec{x},t)$, $\vec{x} \in D, t \geq 0$ denotes the velocity around a rotorcraft as a function of the position, $\vec{x}$ and time, t and D is the flow-field domain:

$$\vec{u}(\vec{x},t) = \vec{u}_{ext}(\vec{x},t) + \vec{u}_{solid}(\vec{x},t) + \vec{u}_{near-wake}(\vec{x},t) + \vec{u}_{far-wake}(\vec{x},t) \qquad \ldots (1)$$

In Equation (1), $\vec{u}_{ext}$, $\vec{u}_{solid}$, $\vec{u}_{near-wake}$ and $\vec{u}_{far-wake}$ are, respectively, the specified external velocity for the given flight condition, the velocity due to the influence of solid bodies such as rotorblades, fuselage, and stabilisers, the velocity due to the influence of the near-wake and the velocity due to the far-wake. Using a panel method approach, $\vec{u}_{solid}$, $\vec{u}_{near-wake}$ and are given in terms of singularity distributions over the surface of the solid bodies extended to a 'near wake', defined as shown in Fig. 1.

Next, the Biot-Savart law provides means for obtaining $\vec{u}_{near-wake}$, where $\vec{\omega}(\vec{x}_0,t)$ is the vorticity vector associated with a singularity at $\vec{x}_0$:

$$\vec{u}_{far-wake}(\vec{x},t) = \int_{D(t)} \frac{\vec{\omega}(\vec{x}_0,t) \times (\vec{x} - \vec{x}_0)}{4\pi |\vec{x} - \vec{x}_0|^3} \, dD \qquad \ldots (2)$$

Following the panel method calculations at a given time step, the 'near-wake' strip elements are transformed into vortex particles and become part of the 'far-wake.' Integrating the vorticity of each near-wake dipole element produces a vortex particle. The new vortex particles become part of the far wake, which evolves prior to the next time step using a description of the flow. Figure 1 gives a schematic of the so-called 'vortex blobs' formation process. Details of the aerodynamic model can be found in other publications[1,4]. Figure 2 shows a visualisation of the wake produced by a typical rotor in forward flight, at an advance ratio of 0·14 using GENUVP. The formation and expansion of tip vortices at the edges of the rotor disc are visible.

Figure 3 shows a comparison of the final solution for blade spanwise loading in hover. The comparison results are from a CAMRAD II simulation, run as part of the analysis done by Shin[11]. The two codes predict a similar spanwise load distribution, which increases with radial distance. Both codes predict a peak in the spanwise loading between the stations 90% and 100% of the radius. The difference in the magnitude of the predicted peaks is attributed solely to the different wake geometries modelled by the two codes: specifically, the difference in the amount of wake contraction. It should be noted that the amount of wake contraction in CAMRAD II is based on a parameter calculated from the measured wake geometry, obtained from an experiment[12] not available in the present case.

Figure 4 shows a comparison of the total lift loading for a single blade over a period of two complete rotor revolutions. Likewise in the previous case the comparison is against results obtained by Shin[11] using Peter and his finite-state induced flow model[13].

For the latter result, both codes compare favourably in terms of overall trends. The seen differences can mainly be attributed to the wake modelling, as GENUVP is able to capture higher frequency loading variations than a finite-state induced flow model.

2.2 Structural component

Hodges used a mixed variational approach to develop a 'geometrically exact' formulation for the dynamics of rotating beams[3]. Hodges' formulation decomposes the analysis of the three-dimensional blade structure into a linear analysis of the cross-section geometry and material properties, and a non-linear one-dimensional analysis along the beam reference line. A geometrically exact description of the beam reference line makes Hodges' formulation
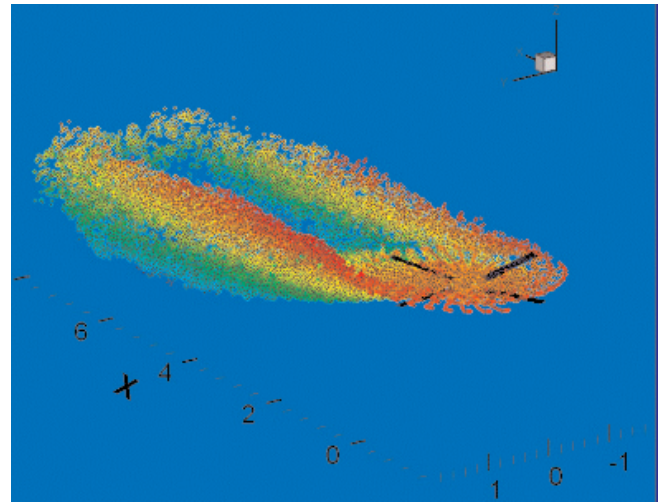

Figure 2. Visualisation of the free wake produced by a typical four-bladed rotor in forward flight[4].
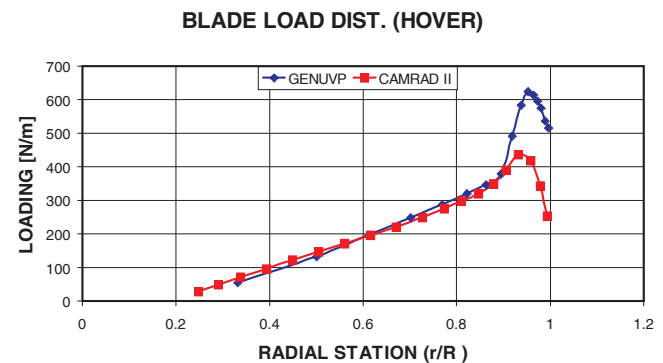
BLADE LOAD DIST. (HOVER)

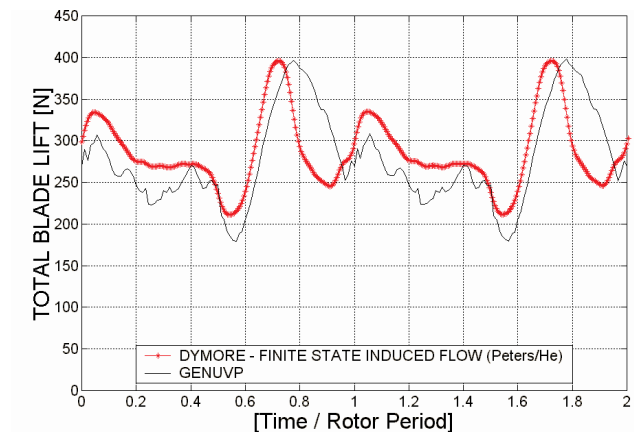Figure 3. Blade spanwise loading of a typical blade in hover[4].

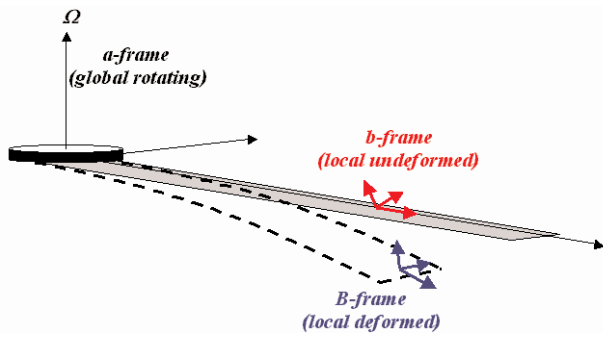Figure 4. Total lift loading on a single blade in forward flight[4].

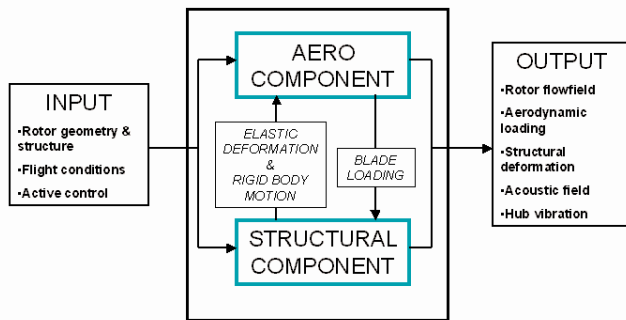Figure 5. A schematic diagram of the co-ordinate frames used by the structural component.

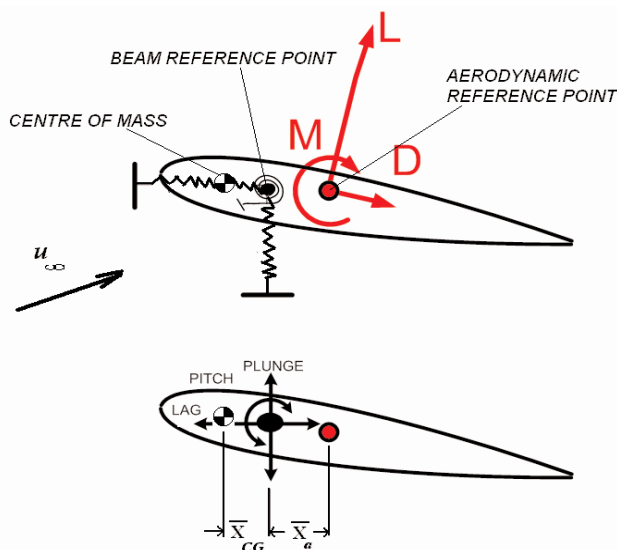Figure 6. Basic components of the code.

Figure 7. Schematic diagram of the basis for aeroelastic coupling of the aerodynamic and structural components.

suitable for capturing the large deformations that rotor blades typically experience. In addition, Hodges' formulation uses full constitutive relations for elastic and inertial properties, allowing capture of the coupling between the beam degrees of freedom. Shang[14] extended Hodges' work by writing the mixed variational equations of motion in a global rotating frame, and applying the finite element method for the spatial discretisation. In the latter formulation, three co-ordinate frames were used in the equations of motion: (1) global, a, (2) local non-deformed, b and (3) local deformed, B. A diagram of the co-ordinate frames is shown in Fig. 5, where a follows the blade around the rotor azimuth angle and b describes the local non-deformed orientation of the blade reference line as a function of a spanwise curvilinear co-ordinate. The latter frame accounts only for the initial curvature and pre-twist of the blade, and it can be related to frame a through direction cosine transformations. Frame B describes the locally deformed orientation of the beam reference line. This frame includes both rigid and elastic rotations due to arbitrarily large angles. The use of these three reference frames allows a compact, 'geometrically exact,' beam formulation, while also allowing the use of constitutive relations solely based on the deformed reference frame, B. The original work by Shang[14] contains details of this analysis.

Adopting the finite element method, the spatial domain of the blade is discretised into N spanwise elements. Once the discretisation is applied, a set of non-linear partial differential equations in time are obtained:

$$F_S\left(X, \dot{X}\right) - F_L = 0 \qquad \qquad \ldots (3)$$

In Equation (3), F_S is the structural operator, F_L is the load operator, and $\mathbf{X}$ is the unknown vector consisting of structural variables; namely discrete measures of displacement, rotation, internal loads, moments, and selected boundary values. It is worthwhile to stress that in this formulation the form of $\mathbf{X}$ depends on the type of rotor boundary conditions being considered. For example, for the hingeless rotor tested in the HELINOISE program, the unknown boundary quantities included in $\mathbf{X}$ are the blade root forces and moments and the blade tip displacements and rotations. Equation (3) gives a geometrically exact description of the dynamics of a rotating beam. To apply a numeric method to solve these equations, two main considerations are necessary; namely, a method for computing the derivatives, and a scheme for solution of the non-linear equations of motion. Cheng[2] developed a structural code based on Shang's formulation[14]. The structural code solves the non-linear equations of motion in a time-marching fashion. An Euler-based, second-order backward finite difference scheme is applied to numerically approximate the derivatives in Equation (3) and solve iteratively for the $\mathbf{X}$ vector of unknowns. Further details of the method and the validations associated with the structural component are found in a previous work[15].

2.3 Aeroelastic coupling

The two separate components of the rotor (aerodynamic and structural) are formulated and solved independently. At each time step, aeroelastic data consisting of loads, aerodynamic damping, deformation, and deformation rates are exchanged between the two components, as shown in Fig. 6. This process is repeated until a periodic solution is found in the time domain.

The aeroelastic coupling between the aerodynamic and structural components is based on an extension of the simple aeroelastic problem of a two-dimensional aerofoil section, depicted in Fig. 7. In this figure, the aerofoil section is shown with degrees of freedom in the plunge (vertical), lag (horizontal), and pitch (rotational) degrees of freedom. These degrees of freedom are elastically restrained, represented in Fig. 7 by linear and torsional springs at the beam reference point. Offsets between both the beam reference axis and
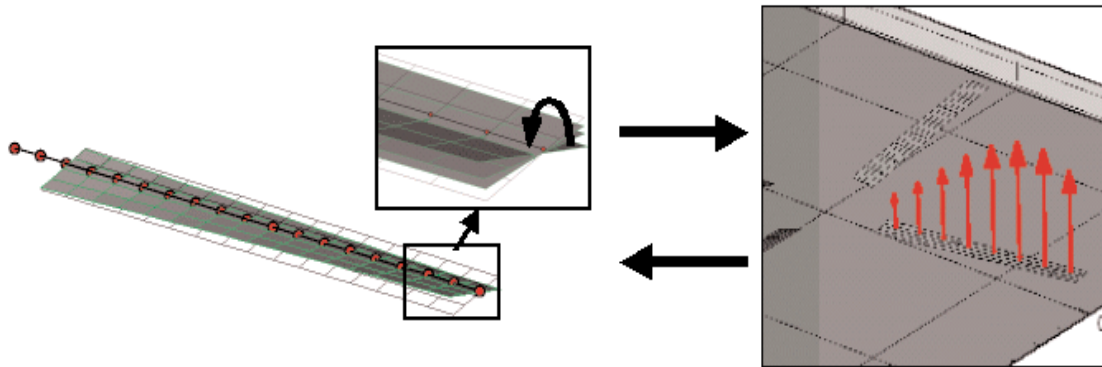
Figure 8. Schematic diagram of the code aeroelastic coupling method.

aerodynamic centre, $\overline{X}_a$ and centre of gravity, $\overline{X}_{CG}$ are considered. $\vec{u}_\infty$ is the undisturbed flow velocity vector). This system is extended to three dimensions as at every blade section the loading, including the effect of elastic velocity and rotation about the beam reference axis, is computed by the aerodynamic component. Although the structural component has six degrees of freedom at each spanwise node, only two displacements and one rotation, namely; the plunge (flap), lag and pitch degrees of freedom are considered for aeroelastic coupling.

By extending the two-dimensional aeroelastic system to three dimensions, a framework is developed for coupling the aerodynamic and structural components, as shown schematically in Fig. 8.

The structural and aerodynamic components retain in the code separate representations of the blade. The structural component uses a one-dimensional beam-element discretisation of the beam reference axis, typically from the hub attachment point to the blade tip. The aerodynamic component models the three-dimensional lifting surface of the blade as panel elements. Each section of the three-dimensional blade bears a similar representation of the aeroelastic problem shown in Fig. 7, where the effective section loading and elasticity are provided by the aerodynamic and structural components, respectively. The aerodynamic component solves for the potential loading L at every spanwise station. Using L, the effective section angle-of-attack fully including the unsteady free-wake effects is calculated. Next, using aerofoil lookup tables the section drag, D is obtained to account for the viscous effects not captured by the potential theory. The pitching moment coefficient in the present work is also obtained from aerofoil lookup tables to avoid the need for a very fine discretisation near the aerofoil leading edge, further reducing the computational costs, although this simplification is not required by the code. The aerofoil tables are typically indexed by both angle-of-attack and section Mach number, therefore allowing for compressibility corrections. The spanwise loading distribution is then applied to the beam reference axis to solve for the aeroelastic response. The elastic deflections obtained from the latter are used to deform the aerodynamic mesh of the lifting surface, as depicted in Fig. 8. In this process, the rate of elastic deformation of the blade provides an additional body velocity component that needs to be accounted for in the non-penetration condition in the aerodynamic formulation.

2.4 Aeroacoustic component

Ffowcs-Williams and Hawkings derived the FW-H equation based on the Lighthill acoustic analogy[5]. The FW-H equation treats the problem of sound generated by a body in arbitrary motion in a fluid as a problem of mass and momentum conservation, with a mathematical surface discontinuity corresponding to the body surface. Outside of the surface, the exterior flow field defines the domain; the flow on the interior of the surface is arbitrary (although, typically, assumed to be at rest). Mass and momentum sources are used to create the surface discontinuity, and ultimately act as sound generators. The acoustic analogy is then applied to obtain the governing equation of the problem.

The fluid mass and momentum conservation equations are written next, including the surface discontinuity, and combined to obtain a wave equation. Letting $\vec{x}$ and $\vec{y}$ be the observer and source position vectors, respectively, and $f(\vec{y},t) = 0$ describe the motion of the surface of a body, the FW-H equation reads[5]:

$$\left(\frac{1}{c^2}\frac{\partial^2}{\partial t^2} - \nabla^2\right)p' = \frac{\partial}{\partial t}\left[\rho_o v_n |\nabla f| \delta(f)\right]$$
$$- \frac{\partial}{\partial x_i}\left[l_i |\nabla f| \delta(f)\right] \qquad \dots (4)$$
$$+ \frac{\partial^2}{\partial x_i \partial x_j}\left[T_{ij} H(f)\right]$$

Equation (4) gives the sound generated by the body moving through a fluid, where p' is the acoustic pressure measured at the observer position, $\vec{x}$; c and ρ_0 are the speed of sound and the density of the undisturbed medium, respectively; v_n is the local normal velocity on the body surface, l_i is the local force on the fluid per unit area, and T_{ij} is the Lighthill stress tensor; $\delta(f)$ and $H(f)$ are the Dirac delta and Heaviside functions, respectively.

The three terms on the right-hand side of Equation (4) are associated to the fluid thickness (monopole), loading (dipole), and shear deformation (quadrupole) noise sources, respectively. The monopole source accounts for noise due to the displacement of the fluid by the finite thickness of the body; the dipole source accounts for noise due to loading and changing of pressure loading on the body, and quadrupole source includes the noise due to compressibility effects such as produced by shock waves. The fluid loading and thickness noises are originated from surface sources, whereas the shear deformation noise is generated from a volume source. In the current formulation, the quadrupole noise source cannot be considered because it requires a volume grid-based flow solver. However, neglecting the quadrupole term is a practical approximation as the monopole and dipole terms dominate all noise generation when the flow is not transonic[16]. Thus, the present
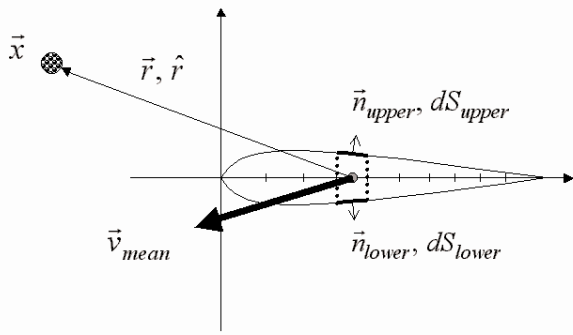
Figure 9. Illustration of the method used to calculate the normal velocity on the actual blade surface.
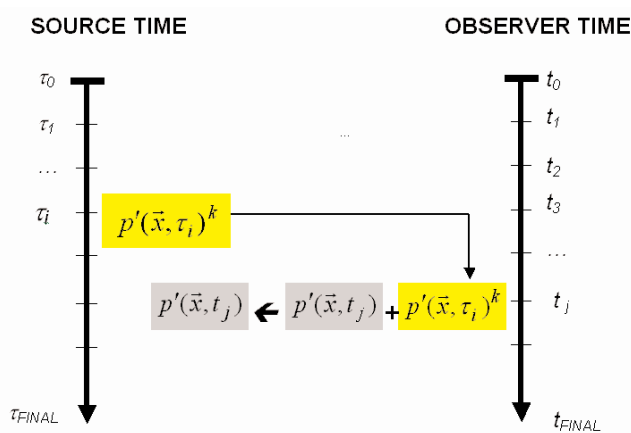

Figure 10. Diagram of the time-shifting scheme used to determine the acoustic pressure history in the observer time scale.

formulation is valuable for a great deal of rotor noise prediction applications, including BVI, which is well known mostly generated at lower advance ratios, in ascending and descending flight rotor operations. Ffowcs-Williams and Hawkings stated that the only restriction placed upon a surface in the FW-H equation is that it should be smooth; otherwise it would be allowed to move in an arbitrary fashion and change its shape or orientation[5]. Therefore, blade flexibility effects can be included in the formulation.

In the current work, an acoustic formulation based on Farassat's 1A solution of the FW-H equation[17] is pursued. The 1A is a solution of the FW-H equation for thickness and loading noise sources obtained by integration on the body surface. The 1A solution is a well-validated method that is being used extensively in rotorcraft aeroacoustics[18,19]. There are enhancements for approximating the quadrupole term, but those were not considered in the present work[20]. As the work by Farassat and Succi[17] contains the complete derivation of the 1A solution, only the final solution is repeated here for the sake of completeness. Equations (5) and (6) produce respectively the loading and the thickness acoustic pressure contributions to the total acoustic pressure, $p'(\vec{x},t) = p'_L(\vec{x},t) + p'_T(\vec{x},t)$ measured at the observer position, $\vec{x}$.
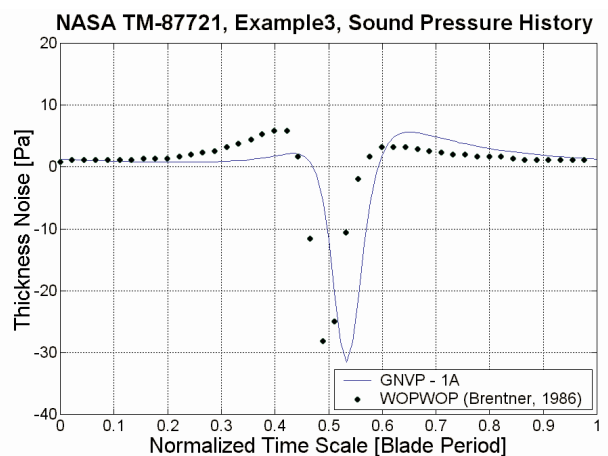
$$4\pi p'_L(\vec{x},t) =$$

$$\frac{1}{c}\int_{f=0}\left[\frac{\dot{l}_i\hat{r}_i}{r\left(1-M_r\right)^2}\right]_{ret}dS \qquad \ldots (5)$$

$$+\int_{f=0}\left[\frac{l_r-l_iM_i}{r^2\left(1-M_r\right)^2}\right]_{ret}dS$$

$$+\frac{1}{c}\int_{f=0}\left[\frac{l_r\left(r\dot{M}_i\hat{r}_i+cM_r-cM^2\right)}{r^2\left(1-M_r\right)^3}\right]dS$$

$$4\pi p'_T(\vec{x},t) = \int_{f=0}\left[\frac{\rho_0 v_n\left(r\dot{M}_i\hat{r}_i+cM_r-cM^2\right)}{r^2\left(1-M_r\right)^3}\right]_{ret}dS \qquad \ldots (6)$$

In Equations (5) and (6), $\vec{r} = \vec{x} - \vec{y}$ is the vector defining the observer and source positions, respectively, $r = |\vec{r}|$, $M_i = v_i/c$ is the local Mach number, $M_r = M_i\hat{r}_i/r$ is the radial Mach number and $l_r = l_i\hat{r}_i/r$ is the
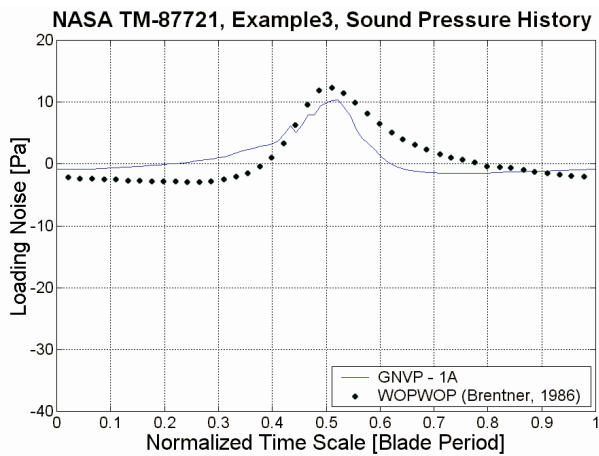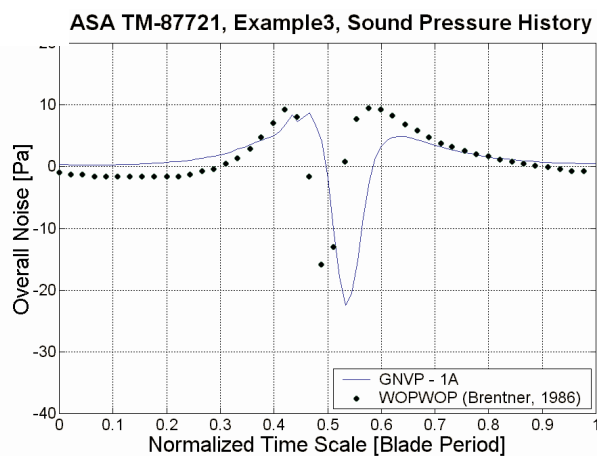

(a) Loading

(b) Thickness

Figure 11. Comparisons of acoustic pressures for the UH-1H rotor in hover:

radial force per unit of area on the fluid. The subscript *ret* indicates that the integrals must be evaluated in the 'retarded time', τ defined by the time at which the acoustic signal was emitted. The hat accent indicates unity vector and dot the derivative with respect to time. The acoustic signal history is measured at the observer position, in the observer time frame, *t*. In the present solution, the integrals shown in Equations (5) and (6) are numerically evaluated by discretising the body surface into elements and adding up the elementary contributions to the two acoustic pressures. The acoustic component of the developed code uses the same discretisation as the aerodynamic component, therefore treating each panel as an acoustic source. After the potential calculations are completed, the aerodynamic results are used to calculate the emitted acoustic signals. At the end of the simulation, the predicted acoustic pressure history at each specified microphone (observer position) is obtained. The loading noise contribution of each panel is calculated as a function of the potential loading, velocity, and distance to the microphone. Viscous corrections are not included. Special consideration is needed for the thickness noise term since thin lifting surface representation is used in the current work, and the thickness noise term is dependant on the local normal velocity on the actual blade surface. Therefore, for each actual panel, projected upper and lower surface 'virtual' panels are determined from the known aerofoil geometry. The normal velocity is then calculated for the upper and lower surface panels using the velocity of the mean surface panel, and the normal vectors of the projected panels, according to Fig. 9. The thickness noise contribution is then evaluated as the sum of the contribution of the upper and lower projected panels.

Once the acoustic pressure contribution of each panel is calculated, the total acoustic pressure history at each microphone is determined by summation, taking into account the time sequencing due to the difference in travel distance for each acoustic emission. Considering Fig. 10, an approximation for the relation between the source time (when the signal is emitted) and the observer time (when the signal is received) is obtained in Equation (7) for the acoustic signal $p'(\vec{x}, \tau_i)^k$ emitted by the kth panel at time τ_i measured in the source time frame, which is identified to the time frame at which the aerodynamic calculations are computed.

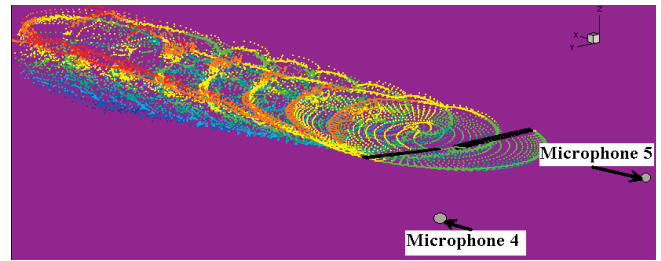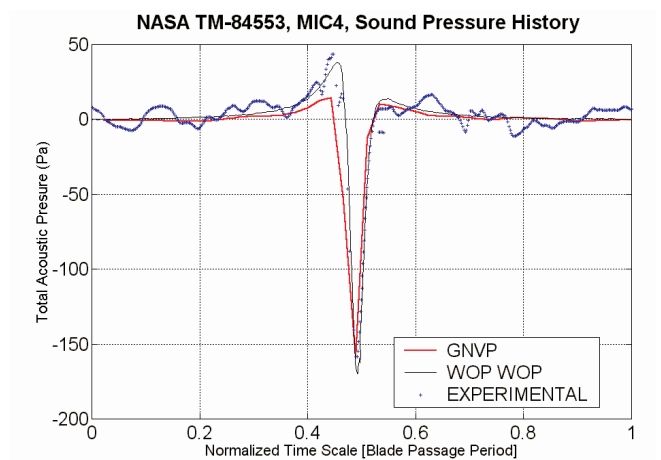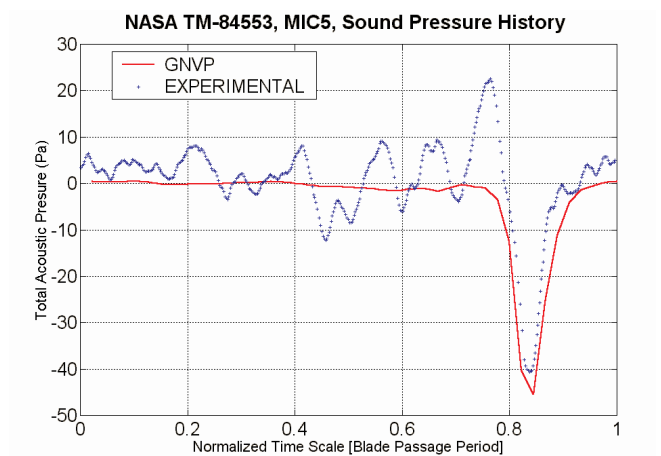$$t_j = \tau_i + \frac{r}{c + \hat{r} \cdot \vec{u}_\infty} \qquad \ldots (7)$$

Figure 12. Visualisation of the wake produced by the UH-1H rotor in forward flight and the locations of Microphones 4 and 5.

(a) Advancing side microphone

(c) Total

Figure 11. continued

(b) Retreating side microphone.

Figure 13. Comparison of total acoustic pressure for the UH-1H in forward flight:
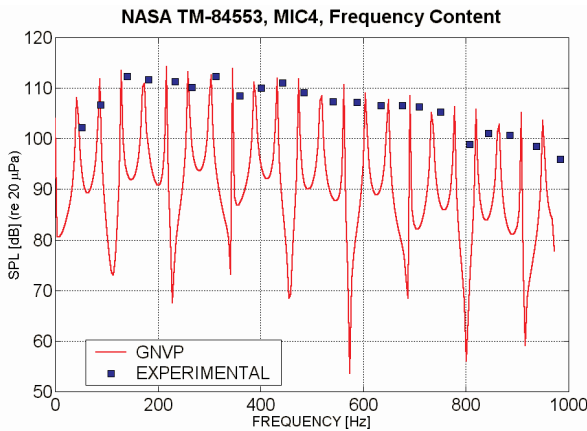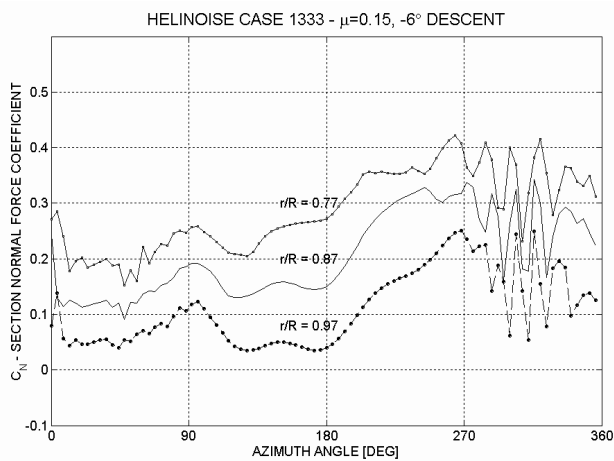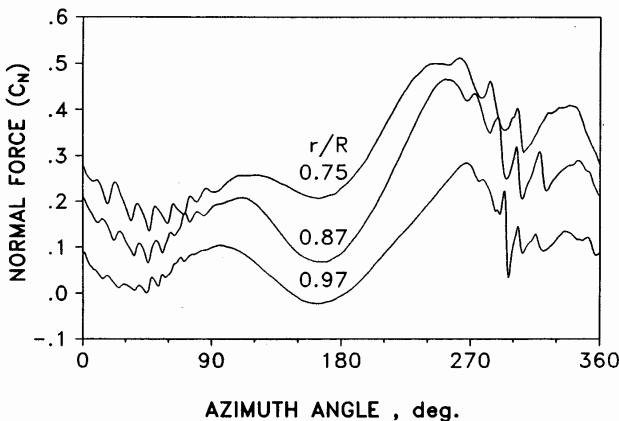
Figure 14. Comparison of frequency content of the total
acoustic pressure prediction of the advancing side
microphone for UH-1H in forward flight.

(a)

(b)

Figure 15. Normal force coefficient for HELINOISE case 1333:
(a) Predicted. (b) Experimental[24].

Table 1
Data summary for the BO105 model rotor

Scaling factor	2·455
Number of blades	4
Rotor type	Hingeless
Aerofoil	NACA 23012 modified
Rotor radius	2m
Blade chord	0·121m
Pre-twist (outboard of 0.44m radius)	–4°/m
Nominal rotor speed	1,050RPM (110rad/s)

For the purpose of validation of the acoustic component alone, the scaled model of the two-bladed teetering UH-1H rotor is used and rigid blade assumption is adopted. Details of the scaled UH-1H rotor are found in the open literature[21]. To accurately capture the acoustic signal, very fine discretisation is required in both space and time. By running repeated test cases, it was found that the time step size to capture the acoustic signal should be at least 90 time steps per revolution (4 degrees azimuth angle discretisation). In contrast, a resolution of 60 time steps per revolution is sufficient to produce accurate aerodynamic results. It was also found that finer chordwise discretisations of the blade at the leading edge are required for producing results independent from panel size. Figures 11(a)-(c) depict comparisons of the loading, thickness, and total acoustic pressures in hover, respectively, measured at a microphone situated three meters from the hub, in the plane of the rotor. Comparison results are from the original version of the code WOPWOP[22], which uses a slightly modified Farassat 1A acoustic formulation. The two codes agree well in all three comparisons. The slight time shift visible in the results is caused by the difference between the two codes of the rotor starting position.

Figure 12 shows a visualisation using the present code of the wake produced by the UH-1H rotor in forward flight (0·208 advance ratio and 8·85° forward disc tilt angle). The location of two microphones where acoustic pressure is computed is also depicted. Microphone 4 is situated four meters ahead of the rotor hub on the advancing side, and Microphone 5 is situated four meters ahead of the rotor hub on the retreating side.

Figures 13(a)-(b) show a comparison of the total acoustic pressures at the two microphone locations. Comparisons are given with both experimental[21] and WOPWOP data[22] for the advancing side microphone, and with experimental data alone for the retreating side microphone. In both cases, the overall trend is captured by the present code. The higher frequency component present in the experimental results is not captured by either code. While some of this high-frequency component may be due to experimental scatter, it is suspected that the oscillations may be due to blade flexibility.

Figure 14 depicts a comparison of sound pressure level, SPL versus frequency for the microphone on the advancing side of the rotor against the experiment results[21]. The peaks in SPL at harmonics of the blade passage frequency are accurately captured by the present code. The overall trend of the frequency spectrum was captured as well.

Table 2
Summary of inertial and elastic properties used in the present work

m	0·948 kg/m
I_{11}	6·23 10^{-4} kg-m^2/m
I_{22}^*	8·89 10^{-6} kg-m^2/m
I_{33}^*	6·10 10^{-4} kg-m^2/m
EA^*	1·64 10^6 N
GJ	2·50 10^2 N-m^2
EI_{FLAP}	1·90 10^2 N-m^2
EI_{LAG}	4·71 10^3 N-m^2

3.0 COMBINED CODE RESULTS AND VALIDATION

In the HELINOISE program, a scaled model of the main rotor of an ECD BO105 four-bladed hingeless helicopter was tested[23]. A summary of rotor data for the BO105 model is presented in Table 1. The test rotor was scaled forty-percent geometrically, in addition to Mach number and blade dynamics. One of the test rotor blades was extensively instrumented with pressure transducers to measure aerodynamic loads, and with strain gauges to measure the blade flapping, lead-lagging, and torsional deformation. The HELINOISE test was conducted in the German-Dutch Wind Tunnel[24],

A transverse microphone array was used during the experiment to measure the rotor acoustic signature on a plane below the rotor. The HELINOISE test plan included hover, level flight, climb and descent conditions, over a range of advance ratios. Particular attention was paid to descent flight conditions to capture BVI event test data.

Although effort was made to model the HELINOISE test set-up in the present validations as close as possible, certain approximations were necessary due to lack of availability of detailed blade structural data and for simplification purposes. Only the lifting surfaces of the blades are modelled with both the structural and aerodynamic components, with a cantilevered root boundary condition for both the blade flapping and lead-lagging motions. This simplification means that the present model does not include the effects of flexibility of the existing blade root cutout. The fuselage present in the tests is not considered in the present model, which would have some effect on the aerodynamic results due to changes in the inflow, and on the acoustic results due to acoustic shielding of microphones. Finally, due to lack of availability of detailed blade construction information, some of the structural input data are estimated by comparison with similar aeroelastically scaled model rotors. Table 2 gives a summary of the blade section inertial and elastic properties used in the present analysis. An asterisk denotes properties that are estimated using indirect data. The blade reference axis is taken at 21% of the chord.

The present paper includes the predictions for the HELINOISE test case 1333 (Low-speed descent (0·15 advance ratio, −6° flight path angle). Results for additional test cases can be found in another work[4]. The test cases demanded a total simulation length of approximately 18 rotor revolutions. Over the first three revolutions, the loads transferred to the structural component are linearly increased to minimise structural transient oscillation due to the impulsive starting of the rotor. To
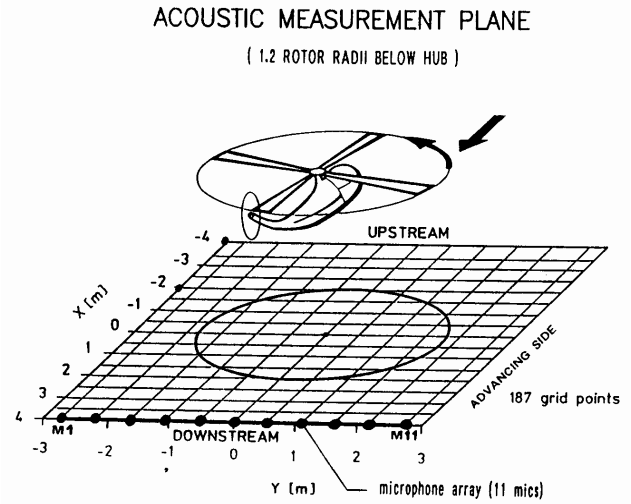

Figure 16. HELINOISE acoustic measurement plane relative to the model rotor. Microphone positions[24].

allow this initial structural transient response to decay, ten revolutions are then used from the time of full load application to the start of particle wake activation. The particle wake is activated during the final five revolutions. The results became periodic prior to the final three revolutions. A typical run takes about 48 hours in a single processor desktop personal computer equipped with a 2GHz clock.

3.1 Aerodynamic loading

The normal force coefficient (integration of blade pressure) is measured on a radial section of the blade, normal to the section chord. The normal force coefficient can be used to detect blade-vortex interaction (BVI) encounters. Theoretically, BVI is expected in the first and last quadrant of the azimuth cycle. Figure 15(a) shows the predicted normal force coefficient history at the outer portion of the blade, for
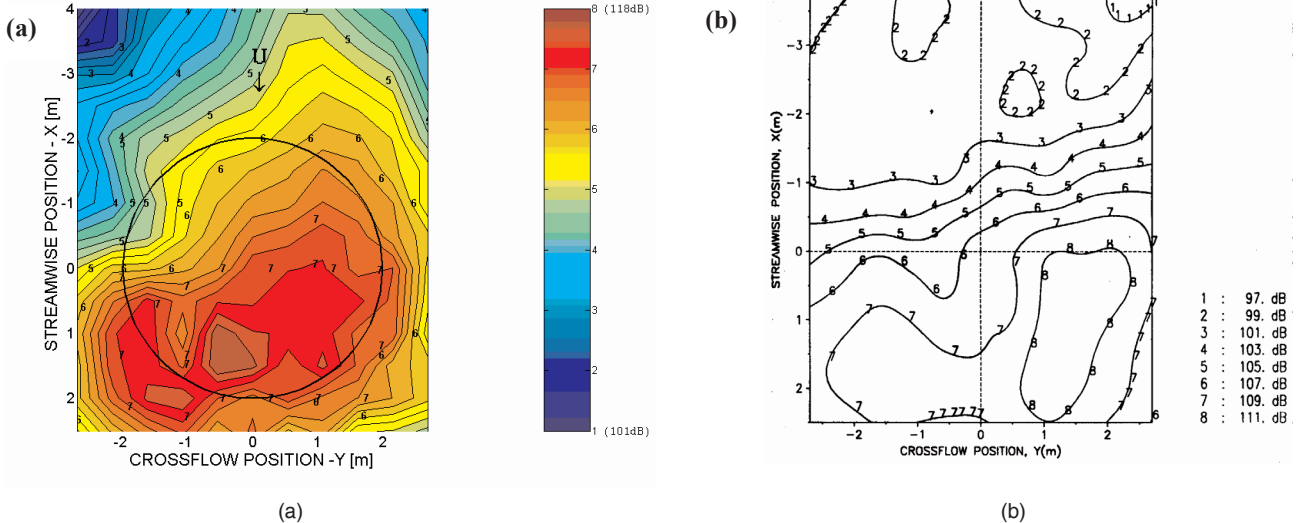

Figure 17. Low-frequency summary level plots (up to the 10th harmonic) for HELINOISE case 1333: (a) Code predictions. (b) Experimental[24].

one revolution, for HELINOISE case 1333; Fig. 15(b) shows the experimental results for the same case. The present code accurately predicts the overall trend and magnitude of the normal force coefficient history. In addition, the BVI events on the advancing and retreating sides are captured. The magnitude of the predicted BVI on the retreating side is larger than the corresponding experimental measurement.

3.2 Acoustic results

During the HELINOISE experiment, the acoustic signals were measured on a plane at approximately 1·2 rotor radii below the rotor hub, as shown in Fig. 16. Collecting data on such a grid allows a comprehensive evaluation of the intensity and directivity of noise produced by the rotor. An acoustic grid that matches the points that were used in the HELINOISE experiment is specified for the present model for test case 1333.

The HELINOISE experimental acoustic measurements were reduced to a single acoustic measurement index called the frequency summary level or FSL for each microphone location[23]. Using a Fast Fourier Transform, data were converted into a narrowband frequency versus magnitude spectrum. The magnitude was expressed on a decibel scale. This spectrum had distinct tones at harmonics of the blade passage frequency. Frequency summary levels were obtained by adding the sound pressure levels of harmonics within a selected frequency range. The low-frequency summary level (LFSL) included harmonics up to the 10th of the blade passage frequency, and this was defined in the project as the

index of the impulsive noise, $LFSL = 10\log\left(\sum_{i=1}^{10} 10^{SPL_i/10}\right)$. By computing

the LFSL on a grid such as that used in the HELINOISE experiment, contour plots are produced in the present work giving an indication of the noise intensity and directivity prediction capabilities of the present code. The predicted LFSL value is calculated for each microphone and the summation taken up to the tenth harmonic.

Figure 17(a) shows the LFSL contour plot for HELINOISE case 1333, produced using acoustic pressure result predictions from the present code. A projection of the rotor circumference is shown with a black circle. Figure 17(b) is the LFSL plot for the same case, produced with measured results. The code predictions display similar directivity and intensity trends as the measured results. The numerical results predict a similar intensity range over the extent of the comparison range, but are slightly higher. The region of high noise intensity is correctly predicted downstream of the hub, within the projected rotor area. An intensity gradient is visible just upstream of the rotor hub, slanted in the cross flow direction. The predicted gradient is more slanted than the measured gradient. Differently from the measured results, peaks are predicted on the retreating side, downstream the hub. These peaks are consistent with the over-prediction of BVI intensity on the retreating side, discussed before. Although the predicted LFSL plot is respectable, results are expected to improve by decreasing the simulation time step size in order to capture the acoustic signals with better resolution. Time-domain comparisons are presented in Appendix A.

4.0 CONCLUSIONS

A new code to predict the aeroelastic and aeroacoustic behaviour of helicopter rotors has been developed. The acoustic component has been designed for predicting the thickness and loading acoustic pressure histories for rotors in hover and forward flight. The acoustic component predictions have been validated both in the time and frequency domains by comparison with computational and experiment data available, including the HELINOISE experiment. The code predictions produced magnitudes and trends similar to experimental results. A respectable capability for prediction of the rotor acoustic signature and blade aerodynamic loading of a rotorcraft has been demonstrated in the paper.
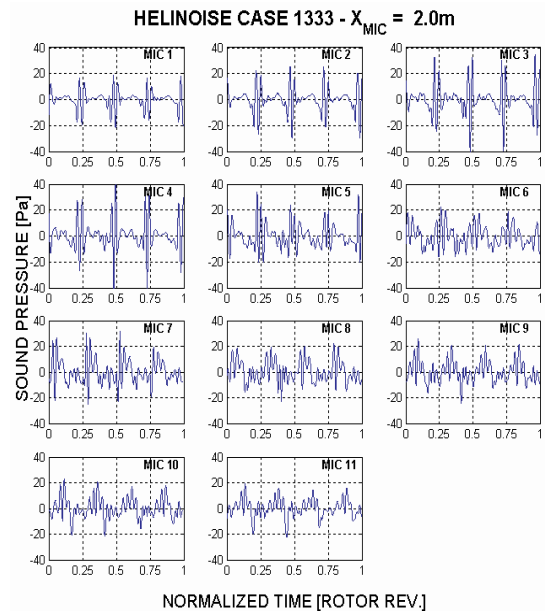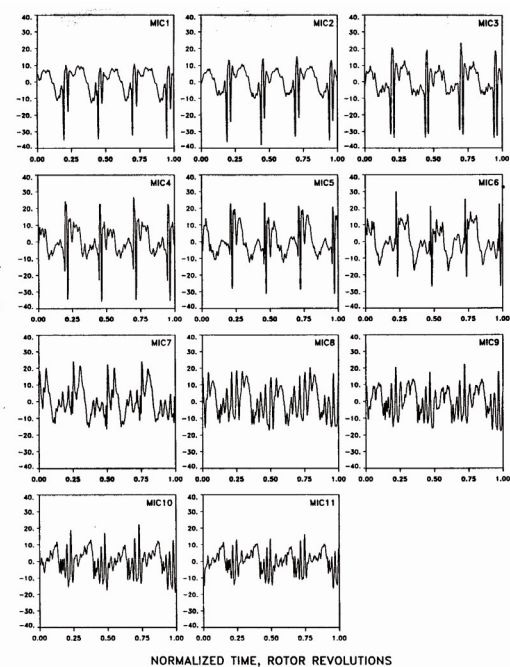
REFERENCES

Figure A1.

Figure A2.

1. VOUTSINAS, S.G. A GENeralized Unsteady Vortex Particle method (GENUVP) for solving the unsteady flow around multi-component configurations, 1990, Report, Dept. of Mechanical Engineering, Fluids Section, National Technical University of Athens, Greece.
2. CHENG, T. Structural Dynamics Modeling of Helicopter Blades for Computational Aeroelasticity, 2002, Master's of Science Dissertation, Massachusetts Institute of Technology, Cambridge, MA.
3. HODGES, D.H. A mixed variational formulation based on exact intrinsic equations for dynamics of moving beams, *Int J solids and structures*, 1990, **26**, (11), pp 1253-1273.
4. OPOKU, D.G. Aeroelastic and Aeroacoustic Modelling of Rotorcraft, 2002, Master of Applied Science Dissertation, Dept of Mechanical and Aerospace Engineering, Carleton University, Ottawa, Canada.
5. FFOWCS-WILLIAMS J.E. and HAWKINGS, D.L. Sound generation by turbulence and surfaces in arbitrary motion, 1969, Philosophical Transactions of the Royal Society, A264.
6. STRAWN, R.C. and DJOMEHRI, R.C. Computational modelling of hovering rotor and wake aerodynamics, Proc 57th AHS Annual Forum, Washington, DC, 9-11 May 2001, pp 1723-1734.
7. PAHLKE, K. and CHELLI, E. Calculation of multibladed rotors in forward flight using a 3D Navier-Stokes method, Proc 26th European Rotorcraft Forum, The Hague, Netherlands, 26-29 September 2000.
8. VOUTSINAS, S.G. and TRIANTOS, D.G. High-resolution aerodynamic analysis of full helicopter configurations, 14-16 September 1999, Proc.25th European Rotorcraft Forum, Rome, Italy.
9. VOUTSINAS, S.G. and TRIANTOS, D.G. Aeroacoustics of full helicopter configurations using vortex particle flow approximations, Proc. CEAS Forum on Aeroacoustics of Rotors and Propellers, 9-11 June 1999, Rome, Italy.
10. VOUTSINAS, S.G., BELESSIS, M.A. and RADOS, K.G. Investigation of the yawed operation of wind turbines by means of a vortex particle method, 1995, Report AGARD CP552, Proc. FDP Symposium on Aerodynamics and Aeroacoustics of Rotorcraft, Berlin, Germany.
11. SHIN, S. Integral Twist Actuation of Helicopter Rotor Blades for Vibration Reduction, 2001, PhD dissertation, Dept of Aeronautics and Astronautics, Massachusetts Institute of Technology, Cambridge, MA.
12. JOHNSON, W. Rotorcraft aerodynamics models for a comprehensive analysis, 1998, Proc American Helicopter Society 54th Annual Forum, Washington, DC, 20-22 May.
13. PETERS, D.A. and HE, C.J. 1995, Finite state induced flow models part II: Three-dimensional rotor disk, *J Aircr*, **32**, (2), pp 323-333.
14. SHANG, X. Aeroelastic Stability of Composite Hingeless Rotors With Finite-State Unsteady Aerodynamics, 1995, PhD dissertation, School of Aerospace Engineering, Georgia Institute of Technology, Atlanta, GA.
15. OPOKU, D.G., NITZSCHE, F., CHANG, T. and CESNIK, C.S. Aeroelastic modeling of active twist rotorblades using particle-wake aerodynamics and Non-linear beam structural dynamics, Paper IMECE 2002-32961, Proc 2002 ASME International Mechanical Engineering Congress and Exposition, New Orleans, LA, November 17-22.
16. BRENTNER, K.S. Modeling aerodynamically generated sound: recent advances in rotor noise prediction, Paper AIAA 2000-0345, 38th Aerospace Sciences Meeting and Exhibit, 10-13 January 2000, Reno, NV.
17. FARASSAT, F. and SUCCI, G.P. The prediction of helicopter rotor discrete frequency noise, 1983, *Vertica*, **7**, (4), pp 309-320.
18. SCHULTZ, K.J. *et al*, Aeroacoustic calculation of helicopter rotors at DLR, Report AGARD CP552, Proc FDP Symposium on Aerodynamics and Aeroacoustics of Rotorcraft, Berlin, Germany, 10-13 October 1994.
19. BEAUMIER *et al*, Effect of higher harmonic control on helicopter rotor blade-vortex interaction noise: prediction and initial validation, 10-13 October 1994, Report AGARD CP552, Proc FDP Symposium on Aerodynamics and Aeroacoustics of Rotorcraft, Berlin, Germany.
20. BRENTNER, K.S. An efficient and robust method for predicting helicopter high-speed impulsive noise, 1997, *J Sound and Vibration*, **23**, (1), pp 87-100.
21. CONNER D.A. and HOAD, D.R. Reduction of high-speed impulsive noise by blade planform modification of a model helicopter rotor, 1982, NASA TM-84553, Langley Research Center, Hampton, VA.
22. BRENTNER, K.S. Prediction of helicopter rotor discrete frequency noise: A computer program incorporating realistic blade motions and advanced acoustic formulation, 1986, NASA TM-87721, Langley Research Center, Hampton, VA.
23. KLOPPEL, V. *Helicopter and Tilt-Rotor Aircraft Exterior Noise Research (HELINOISE), Advances in Acoustics Technology*, 1995, John Wiley and Sons, New York, NY.
24. SPLETTSTOESSER, W.R. *et al*, The HELINOISE Aeroacoustic Rotor Test in the DNW – Test Documentation and Representative Results, 1993, DLR-Mitt. 93-09, German Aerospace Center, Braunschweig, Germany.

APPENDIX A: TIME-DOMAIN RESULTS

Figure A1 shows the predicted acoustic signal with the transverse microphone array, 2m downstream of the rotor hub for HELINOISE case 1333. Microphone 1 is on the retreating side, with the microphone numbers increasing to Microphone 11, which is on the advancing side. For comparison, the experimentally measured results are shown in Fig. A2. Both results present a periodic signal that repeats four times per revolution, corresponding to the blade passage frequency. The predicted acoustic signals are similar to the measured acoustic signals in terms of waveform and magnitude. The similarity along the span of the microphone array indicates the capture, by the present code, of the directivity of the rotor noise. A primary difference between the numerical and measured results is that the impulsive pressure peaks, of the microphones on the retreating side, are not consistently predicted. This is likely due to a truncation error, which could be resolved by using a smaller time step size, to capture the impulsive nature of the acoustic signal